The Astrophysical Journal, 910:146 (11pp), 2021 April 1 https://doi.org/10.3847/1538-4357/abe62a

Core Mass Estimates in Strong Lensing Galaxy Clusters Using a Single-halo Lens Model

J. D. Remolina González[1], K. Sharon[1], N. Li[2,3], G. Mahler[1,4,5], L. E. Bleem[6,7], M. Gladders[7,8], and A. Niemiec[1,4,5]
[1] Department of Astronomy, University of Michigan, 1085 South University Avenue, Ann Arbor, MI 48109, USA; jremolin@umich.edu
[2] CAS, Key Laboratory of Space Astronomy and Technology, National Astronomical Observatories, A20 Datun Road, Chaoyang District, Beijing 100012, People's Republic of China
[3] School of Physics and Astronomy, Nottingham University, University Park, Nottingham NG7 2RD, UK
[4] Centre for Extragalactic Astronomy, Department of Physics, Durham University, Durham DH1 3LE, UK
[5] Institute for Computational Cosmology, Durham University, South Road, Durham DH1 3LE, UK
[6] Argonne National Laboratory, High-Energy Physics Division, Argonne, IL 60439, USA
[7] Kavli Institute for Cosmological Physics, University of Chicago, 5640 South Ellis Avenue, Chicago, IL 60637, USA
[8] Department of Astronomy and Astrophysics, University of Chicago, 5640 South Ellis Avenue, Chicago, IL 60637, USA

Received 2020 August 26; revised 2021 January 21; accepted 2021 February 11; published 2021 April 6

Abstract

The core mass of galaxy clusters is an important probe of structure formation. Here we evaluate the use of a single-halo model (SHM) as an efficient method to estimate the strong lensing cluster core mass, testing it with ray-traced images from the Outer Rim simulation. Unlike detailed lens models, the SHM represents the cluster mass distribution with a single halo and can be automatically generated from the measured lensing constraints. We find that the projected core mass estimated with this method, $M_{\rm SHM}$, has a scatter of 8.52% and a bias of 0.90% compared to the "true" mass within the same aperture. Our analysis shows no systematic correlation between the scatter or bias and the lens-source system properties. The bias and scatter can be reduced to 3.26% and 0.34%, respectively, by excluding models that fail a visual inspection test. We find that the SHM success depends on the lensing geometry, with single giant arc configurations accounting for most of the failed cases due to their limiting constraining power. When excluding such cases, we measure a scatter and bias of 3.88% and 0.84%, respectively. Finally, we find that when the source redshift is unknown, the model-predicted redshifts are overestimated, and the $M_{\rm SHM}$ is underestimated by a few percent, highlighting the importance of securing spectroscopic redshifts of background sources. Our analysis provides a quantitative characterization of $M_{\rm SHM}$, enabling its efficient use as a tool to estimate the strong lensing cluster core masses in the large samples, expected from current and future surveys.

Unified Astronomy Thesaurus concepts: Galaxy clusters (584); Strong gravitational lensing (1643)

1. Introduction

Harbored at the high-density knots of the cosmic web, galaxy clusters trace the large-scale structure formation of the universe, making them valuable cosmological laboratories (see reviews by Allen et al. 2011 and Mantz et al. 2014). Their mass function, which connects their observational properties to the underlying cosmology (e.g., Jenkins et al. 2001; Evrard et al. 2002; Corless & King 2009; Pratt et al. 2019; Bocquet et al. 2020), is one of the ensemble properties that cluster-based cosmological studies are pursuing. However, the efficacy of cluster-based cosmological studies is sensitive to sample size and selection function (e.g., Hu 2003; Khedekar & Majumdar 2013; Bocquet et al. 2019) and requires a good understanding of the inherent systematic errors in the mass estimate due to the observed astrophysical properties (Evrard et al. 2002; Allen et al. 2011; Huterer & Shafer 2018). Other cluster properties predicted by cosmological simulations include the radial profiles and concentrations of dark matter halos (Duffy et al. 2008; Meneghetti et al. 2014; Child et al. 2018) and can be directly tested with observations (e.g., Oguri et al. 2012; Merten et al. 2015). An accurate measurement of the mass profile slope of galaxy clusters requires mass proxies that are sensitive to the total cluster mass, as well as mass proxies whose resolution is high enough to probe the innermost hundreds of parsecs.

Gravitational lensing probes the total (dark and baryonic) matter distribution, independent of baryonic physics and cluster dynamical state. Strong gravitational lensing (SL) has the highest resolution at the core of galaxy clusters, where the SL evidence is present; weak lensing (WL) gives an accurate measurement of the total mass at large clustercentric radii. By combining the mass estimate from SL at the core with a mass estimate at large scales from WL or other mass proxies, we can constrain the mass distribution profile from the core to the outskirts and measure profile parameters such as the concentration of the galaxy cluster (e.g., Gralla et al. 2011; Oguri et al. 2012; Merten et al. 2015). Tension between the observations and theoretical expectations of the mass distribution profile of SL galaxy clusters has been reported (e.g., Broadhurst & Barkana 2008; Gonzalez et al. 2012; Meneghetti et al. 2013); however, these studies are limited by small samples and complicated selection functions.

Thousands of SL galaxy clusters are being discovered with current and upcoming large surveys covering a broad wavelength range, detecting clusters out to $z \sim 2$, and addressing challenges due to small sample sizes. These include cluster surveys based on observations with the South Pole Telescope (SPT; SPT-3G, Benson et al. 2014; SPT-SZ 2500 deg^2, Bleem et al. 2015; Bocquet et al. 2019; SPT-Pol 100 deg^2, Huang et al. 2020; SPT-ECS, Bleem et al. 2020), the Atacama Cosmological Telescope (Marriage et al. 2011; Hilton et al. 2018), the Cerro Chajnantor Atacama Telescope (Mittal et al. 2018), Euclid (Laureijs et al. 2011; Amendola et al. 2018), the Vera Rubin Observatory Legacy Survey of Space and Time (LSST; LSST Science Collaboration et al. 2017), and eROSITA (Pillepich et al. 2018). We expect that hundreds of the newly discovered clusters will be strong lenses (LSST Science Collaboration et al. 2009). With an order-of-magnitude increase in sample sizes, an efficient and accurate method will be required in order to measure the mass at the cores of the SL clusters in a timely manner.

The SL-based measurements of the mass distribution at the cores of galaxy clusters typically rely on detailed lensing analyses. A detailed lens model of a cluster with rich SL evidence (e.g., the Frontier Fields; Lotz et al. 2017) can have a high level of complexity requiring a large number of constraints, extensive follow-up observations, computational resources, and multiple iterations to be finalized (e.g., Johnson et al. 2014; Zitrin et al. 2014; Diego et al. 2016; Kawamata et al. 2016; Lotz et al. 2017; Strait et al. 2018; Lagattuta et al. 2019; Sebesta et al. 2019; Raney et al. 2020a). Due to the limited resources and small number of lensing constraints, which is typical for all but the most massive SL clusters (e.g., Sharon et al. 2020), there is a need to investigate efficient methods to estimate the mass at the core of SL galaxy clusters. Remolina González et al. (2020) presented an evaluation of the mass enclosed by the Einstein radius as a zeroth-order method to estimate the mass at the core of galaxy clusters. The limiting factor when using the Einstein radius to estimate the core mass is the assumption of spherical symmetry inherent to this method. In this paper, we investigate a higher-complexity first-order method, which is more complex than the mass enclosed by the Einstein radius but not as expensive as computing a detailed lens model.

The goal of this paper is to evaluate the use of the single-halo model (SHM) as an efficient method to measure the mass at the core of SL galaxy clusters. We measure the scatter and bias in the mass estimate, establish limitations in the use of the SHM, and explore the dependence of the scatter on the properties of the model and the lens-source system. We use the state-of-the-art Outer Rim simulation run (Heitmann et al. 2019), which facilitates a robust statistical analysis that is representative of the universe.

This paper is organized as follows. In Section 2, we describe the lensing algorithm used in our analysis, `Lenstool`, summarize the procedure employed in detailed lens models, and present the SHM. In Section 3, we describe the Outer Rim simulation and detail the simulated sample used in our analysis. In Section 4, we describe the identification of constraints for the SHM, compute the SHM, and measure the aperture mass enclosed within the effective Einstein radius, M_{SHM}. In Section 5, we measure the bias and scatter of M_{SHM}, in comparison to the true mass. In Section 6, we investigate the effects on the SHM of an unknown background source redshift, the lensing geometry of the arc, and the addition of a second multiply imaged source. Last, we present our conclusions and a summary of the evaluation of the SHMs as a mass estimate at the core of galaxy clusters in Section 7.

In our analysis, we adopt a WMAP-7 (Komatsu et al. 2011) flat ΛCDM cosmology as in the Outer Rim simulation: $\Omega_\Lambda = 0.735$, $\Omega_M = 0.265$, and $h = 0.71$. Masses reported in terms of $M_{\Delta c}$ are defined as the mass enclosed within a radius at which the average density is Δ times the critical density of the universe at the cluster redshift.

2. Background: Lens Modeling

Strong lens modeling analyses use the positional and redshift measurements of lensed galaxies (arcs) as constraints to model the underlying mass distribution. We use the publicly available lens modeling algorithm `Lenstool` (Jullo et al. 2007), which has been widely used (e.g., Johnson et al. 2014; Cerny et al. 2018; Paterno-Mahler et al. 2018; Lagattuta et al. 2019; Jauzac et al. 2020; Mahler et al. 2020; Sharon et al. 2020), and its results are similar to other parametric models (Meneghetti et al. 2017; Priewe et al. 2017; Remolina González et al. 2018; Raney et al. 2020b). `Lenstool` uses a Monte Carlo Markov Chain (MCMC) method to explore the parameter space, identify the best-fit values, and estimate the statistical uncertainties in the model. To characterize the mass density distribution, we use a parameterized dual pseudo-isothermal ellipsoid (dPIE; Elíasdóttir et al. 2007) with seven parameters: position (α and δ), ellipticity ($\epsilon = (a^2 - b^2)/(a^2 + b^2)$, where a and b are the semimajor and semiminor axis, respectively), position angle (θ), velocity dispersion (σ), core radius (R_{core}), and truncating radius (R_{cut}). We fix the truncating radius (R_{cut}) to 1500 kpc, since it is far beyond the lensing region and cannot be constrained using the SL evidence. We note that this range resembles the splashback radius (e.g., Umetsu & Diemer 2017; Shin et al. 2019). In the next subsections, we describe the difference between "detailed" models and SHMs and describe the selection of constraints and priors used for the lens modeling procedure.

2.1. Detailed Lens Models

For an in-depth description of the commonly used procedures in detailed parametric lens modeling, we refer the reader to Verdugo et al. (2011) and Richard et al. (2011) and examples by Mahler et al. (2018, 2020), Lagattuta et al. (2019), and Sharon et al. (2020). Detailed lens models use the galaxy cluster redshift and the position and redshift of the arcs as constraints. One or more large cluster-scale profile(s) represent the dark matter halo(s) of the cluster and correlated structure as needed, and multiple galaxy-scale halos represent the galaxy cluster members' mass contribution. The galaxy-scale potential positional parameters are usually fixed to their observed values, and a parameterized mass–luminosity relation is used to set or fit the other parameters. The brightest cluster galaxy (BCG) may be modeled with a separate halo, as we do not expect BCGs to follow the same mass–luminosity relation as the rest of the cluster members.

Compared to the SHMs that will be introduced in the next section, detailed lens models can be highly complex. The complexity adds the flexibility needed in order to trace the substructure in the form of multiple dark matter halos, filaments, contributions from cluster member galaxies, and, in some cases, uncorrelated structure along the line of sight. The versatility of these models has been shown to be a successful tool for a broad range of study, including that of cosmology, galaxy cluster physics, and the highly magnified background universe (e.g., Johnson et al. 2017a; Acebron et al. 2017; Gonzalez et al. 2020). The flexibility of detailed lens models also means that the models are not unique and require care in the construction and evaluation, often multiple statistical assessments are employed to select between models (e.g., Acebron et al. 2017; Paterno-Mahler et al. 2018; Lagattuta et al. 2019; Mahler et al. 2020).

Detailed lens models for galaxy clusters with rich SL evidence require extensive follow-up observations, computational resources, and multiple iterations of the modeling process. The high complexity of the models relies on a large number of free parameters requiring a large number of constraints, i.e., multiply imaged lensed galaxies, whose availability becomes a limiting factor in the modeling process.

2.2. Single Halo Models

The SHMs are similar to their detailed counterparts and use the same type of constraints. The difference in the SHM modeling procedure is that the lens plane is described by a single cluster-scale dark matter halo, while all secondary halos and contributions from cluster member galaxies are neglected. The small number of parameters requires only a handful of constraints, and the model can be computed quickly and with limited human intervention.

We use the same dPIE halos described above, with six free parameters. We use broad priors in the parameters of the dPIE potential: $-8\farcs0 < \alpha,\ \delta < 8\farcs0$; $0.0 < \epsilon < 0.9$; $0° < \theta < 180°$; 50 kpc $< R_{\rm core} < 150$ kpc; and $500\ {\rm km\ s^{-1}} < \sigma < 1500\ {\rm km\ s^{-1}}$.

The outputs of the lens models include the projected mass distribution (Σ), convergence (κ), shear (γ), magnification (μ), critical curves, and predicted location of multiple images. The tangential critical curves (TCCs) and radial critical curves (RCCs) are the theoretical lines of infinite magnification and name the primary direction along which images (arcs) are magnified. The magnification in the tangential direction is computed as follows: $\mu_t^{-1} = 1 - \kappa - \gamma$. In this analysis, we measure the aperture mass enclosed by the effective Einstein radius ($e\theta_{\rm E}$), defined as the radius of a circle with the same area as that enclosed by the TCCs.

3. Simulated Data

To evaluate the SHM method, we use the state-of-the-art, large volume, high mass resolution, *N*-body simulation Outer Rim (Heitmann et al. 2019) with the HACC framework (Habib et al. 2016). The simulation was carried out at the Blue Gene/Q system at Argonne National Laboratory. The large simulation box ($L = 3000\ {\rm Mpc\ h^{-1}}$ on a side) allows for many massive halos in the redshift range of interest ($z \sim 0.1$–0.7) with detailed projected mass distribution profiles representative of the universe.

The Outer Rim simulation has been used to study the dark matter halo profiles of galaxy groups and clusters (Child et al. 2018), evaluate the effects on lensing due to line-of-sight structure (Li et al. 2019), and construct realistic SL ray-traced simulated images (Li et al. 2016). The simulation does not include the baryonic component; while baryons represent a small portion of the mass content of the galaxy cluster, studies have shown that the baryonic component has nonzero effects on the mass distribution and lensing potential. For example, the concentration of dark matter halos is higher when baryons are included in the simulation (Meneghetti et al. 2003; Wambsganss et al. 2004; Oguri 2006; Hilbert et al. 2007, 2008; Wambsganss et al. 2008; Oguri & Blandford 2009). The light due to the baryonic component is also not depicted in the simulated images, i.e., the diffused light from the intracluster medium and stellar population of cluster member galaxies. Fully accounting for these baryonic effects awaits simulations that include baryonic physics in large cosmological boxes.

The galaxy cluster halos used in the analysis were identified using a friends-of-friends algorithm with a linking length of $b = 0.168$, and the surface density was computed using a density estimator. Rangel et al. (2016) showed that the high mass resolution is robust enough to simulate SL in halos with masses $M_{500c} > 2 \times 10^{14}\ M_\odot\ {\rm h^{-1}}$. Following an SPT-like selection function, all halos with $M_{500c} > 2.1 \times 10^{14}\ M_\odot\ {\rm h^{-1}}$ were selected. From this sample, the strong lenses are identified as those having an Einstein radius of at least a few arcseconds, as measured from the average convergence $\langle \kappa(\theta) \rangle = 1$.

The sample details are presented in Remolina González et al. (2020) and summarized here. The sample of simulated SPT-like strong lenses is made up of 74 galaxy cluster halos spanning a redshift range of $z \sim 0.16$–0.67. The redshift range is similar to other SL samples, like that of the Sloan Giant Arc Survey (Gladders et al., in preparation; Sharon et al. 2020). Future studies will extend the redshift range, $z < 1.75$, to better match surveys like the SPT-SZ 2500-Square-Degree survey (Bleem et al. 2015). We adopt the halo masses (M_{200c}) and concentrations (c_{200c}) that were derived by Child et al. (2018).

The lensed simulated images were created through ray tracing using the projected mass distribution of the galaxy cluster following the procedure detailed in Li et al. (2016). We draw redshifts for the background sources following the observed distribution of Bayliss et al. (2011), leading to a simulated source range of $z \sim 1.2$–2.7. The image plane of each cluster field is generated 5–24 times, each realization using a single redshift and unique background source location. A total of 1024 simulated ray-traced realizations were created from the 74 simulated SL galaxy cluster halos. The simulated images have a resolution of $0\farcs09\ {\rm pixel^{-1}}$ and a field of view of 2048×2048 pixels. No additional noise or errors were added, as we use these simulations to investigate the most ideal case rather than creating mock observations that simulate a particular instrument. The background sources were preferentially placed in areas of high magnification, as highly magnified (total magnification >5) arcs are easily detected from ground-based observations. This strategy was chosen in order to mock the selection function of lensing-selected samples, in which lensing clusters were identified based on the appearance of a giant arc in visual inspection of shallow observational data (e.g., Bayliss et al. 2011; Nord et al. 2016, 2020; Sharon et al. 2020; Khullar et al. 2020). The total magnification is defined as the ratio of the area between the image and source planes of the lensed image. Only isolated halo ray tracing is used; no structure along the line of sight was included. Structure along the line of sight is known to affect the lensing potential (e.g., Bayliss et al. 2014; D'Aloisio et al. 2014; Chirivìet al. 2018; Li et al. 2019). A statistical analysis of the line-of-sight effect and lensing systems without dominant giant arcs is left for future work.

We use the redshift and observed image plane positions of the arcs as our constraints for the lens models. We compare the model mass we derive from the SHM method to the projected mass density from the simulation.

4. Methodology

Our analysis of the simulated ray-traced lensed images is guided by the procedures used with observational data. The images are inspected one at a time to identify the multiply imaged morphological features (emission knots) to be used as positional constraints in the lens modeling process. In the case of observational data, visual inspection is also required for spectroscopic follow-up observation of the arcs and cluster members. Here we assume that the redshifts of the arcs and clusters have been measured (see Section 3 and Remolina González et al. 2020). In this section, we provide a description of the identification of the lensing evidence, compute SHMs, and estimate the mass at the core of the galaxy cluster within $e\theta_{\rm E}$.

4.1. Arc Catalog Identification

Identical to the procedure described in Remolina González et al. (2020), we identify the lensing evidence and measure the positional constraints in the simulated lensed images. Lens modelers take advantage of the expected lensing geometry, morphology, and color information to associate sets of multiple images of the same background source. In our analysis, no color information was implemented, so we rely on the morphology and expected lensing geometry for this identification. For each line of sight, we compile a catalog including the positional locations of the arcs (including identified emission knots within each arc) and their redshift. Each identified set of n multiply imaged features contributes $2n - 2$ constraints.

4.2. The SHM Procedure

One of the advantages of the SHM is that it can be automatically computed with minimal human intervention. It requires as input the cluster redshift, initial center position (e.g., the BCG), and positions and redshifts of the arcs. The best-fit lens model is the one that minimizes the scatter between the observed and model-predicted positions of the arcs in the image plane. Since the single dPIE halo has six free parameters, the SHM requires a minimum of six lensing constraints. We find that of the 1024 simulated lensed images, 938 have enough constraints for an SHM to be computed. We note that while this requirement is satisfied, it does not guarantee that the lens model will be fully constrained and in some cases may result in unphysical SHMs, as will be discussed in the next section.

4.3. Assessment of the SHM Success

A quick visual inspection of the resultant critical curve and model predictions with respect to the lensing evidence can provide a critical quality assessment of the SHMs. We inspect each of the generated models and find that in some cases, the SHM does not reproduce the lensing configuration and/or predicts multiple images in areas where no arcs are found. We flag these cases as "failed SHMs" (F-SHMs); such models would not be trusted in a typical observational analysis and would usually require a more involved lens modeling analysis or more constraints to improve the fidelity of the models.

We flagged 201 out of our 938 models as F-SHMs, leaving 737 that pass the visual inspection (P-SHMs); Figure 1 shows representative examples of P-SHMs (top row) and F-SHMs (bottom row). Each of the 74 galaxy clusters still has at least one SHM that passed the visual inspection, with most having nine or more P-SHMs. We note that due to the construction process of our simulated images, i.e., the background sources were preferentially placed in order to produce highly magnified images, the SHM success rate we quote here does not represent the expected success rate in the universe; it is more tuned to resemble the success rate of modeling systems with giant arcs (e.g., Johnson et al. 2017b; Rigby et al. 2018; Sharon et al. 2020; Remolina González et al. 2021, in preparation). We use the fail/pass distinction in Section 5.

We investigate whether the image plane rms (rmsi) can be used as a quantitative quality indicator in lieu of a visual inspection. The rmsi is often used to determine the goodness of fit of lens models; it measures the scatter between the observed and model-predicted image plane locations of lensed features, and in most strong lens modeling algorithms, it is used in the minimization process. We find that the value of the model rmsi is only a weak predictor of the quality of the SHMs. As can be seen in Figure 2, while the highest bins of rmsi are dominated by F-SHMs, both P-SHMs and F-SHMs span the full range of low-rmsi bins. This means that a low rmsi is not a sufficient indicator of model quality. This finding is consistent with previous studies. In an observational analysis of 37 lensing clusters, Sharon et al. (2020) found that while the rmsi serves as a good statistical indicator when comparing different lens models of the exact same system, it is not a good absolute predictor of lens model quality. Johnson & Sharon (2016) used simulations to study the relationship between the rmsi, the number of constraints, and the accuracy in recovering the mass and magnification. They found that, as expected, the accuracy of the magnification and mass recovered by the lens models improved with larger numbers of constraints; however, the rmsi increases with the number of constraints. We therefore do not recommend relying on rmsi alone in order to determine which models pass or fail.

4.4. Aperture Mass Enclosed by $e\theta_E$

We use the projected mass distribution (Σ) from the best-fit lens model to compute other outputs, including the magnification (μ), convergence (κ), and shear (γ). We compute the magnification in the tangential direction (μ_t) and determine the location of the TCC ($\mu_t \rightarrow \infty$). Next, we measure the $e\theta_{\rm E}$ as the radius of the circle with the same area as the area enclosed by the TCC. Last, we measure the aperture mass centered at the center of the modeled dPIE dark matter halo and enclosed by the effective Einstein radius, which we denote as $M_{\rm SHM}$.

4.5. Statistics

To establish a robust statistical analysis using our simulated SL sample, we weight each of the 74 SL galaxy clusters equally. We also weight each ray-tracing realization by a factor of 1 over the total number of realizations with SHMs for each galaxy cluster. Then, for every simulated cluster, we randomly select one $M_{\rm SHM}$ representative of a ray-tracing image. We repeat this process 1000 times for each of the 74 simulated clusters for a total of 74,000 mass measurements used in our statistical analysis.

5. Analysis of Results

In this section, we compare the aperture mass enclosed by the effective Einstein radius of the SHM ($M_{\rm SHM}$) and the "true" mass enclosed within the same aperture from the simulation ($M_{\rm SIM}$). We compute the scatter and bias of $M_{\rm SHM}$ versus $M_{\rm SIM}$ and explore whether the $M_{\rm SHM}$ depends on the lens model parameters and the simulated galaxy cluster properties.

For the statistics used in this analysis, see Section 4.5. The scatter is computed as half the difference between the 84th and 16th percentiles. The bias is computed as

$$\text{bias} = \text{median}(M_{\rm SHM}/M_{\rm SIM}) - 1. \qquad (1)$$

In Figure 3, we plot a direct comparison between $M_{\rm SHM}$ and $M_{\rm SIM}$. We measure an overall scatter of 8.52% about the 1:1 relation between $M_{\rm SHM}$ and $M_{\rm SIM}$ (drawn in Figure 3 to guide the eye) with a positive bias of 0.90%. Interestingly, in the

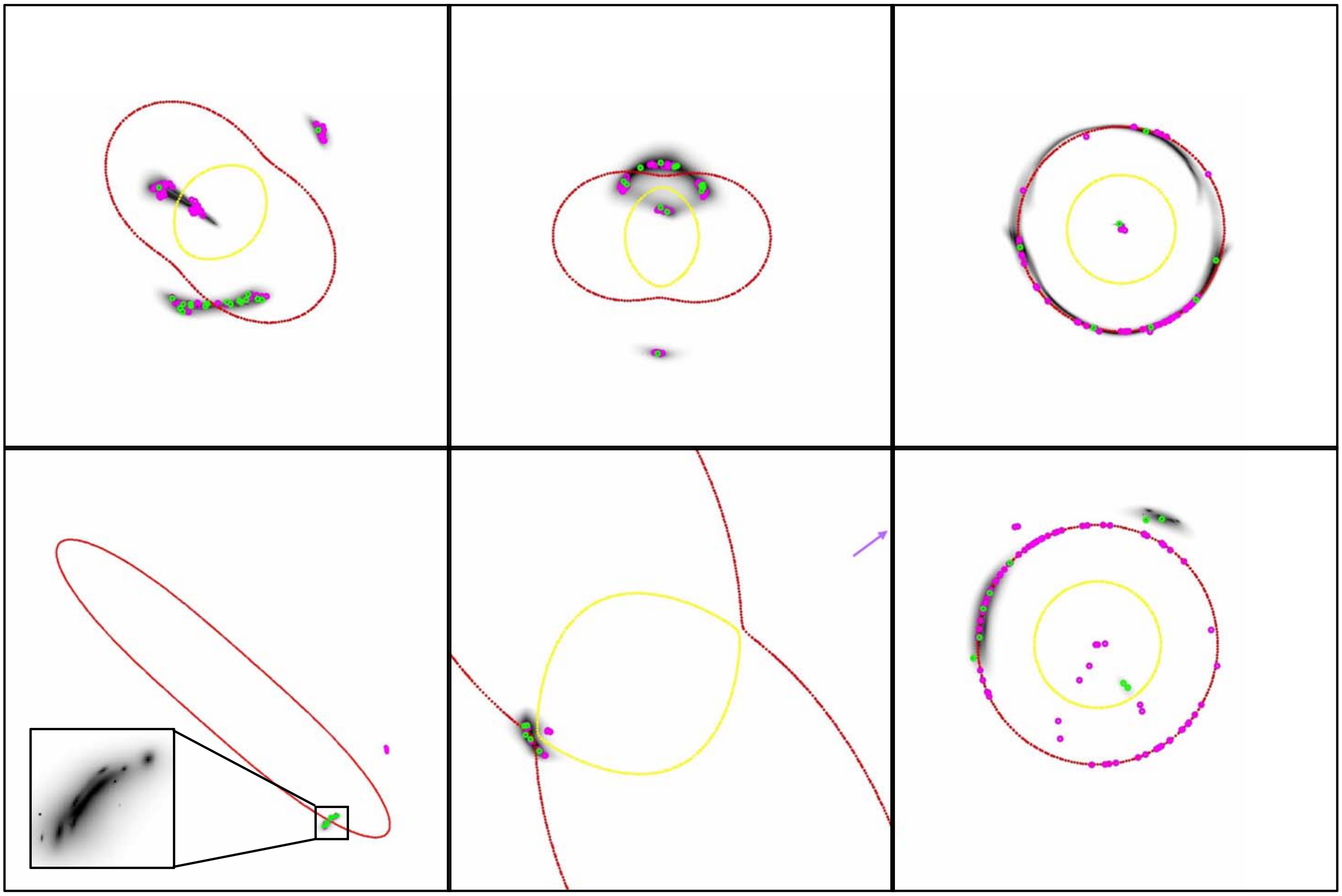

Figure 1. Examples of SHM outputs, overplotted on six ray-traced lensing images. The TCCs and RCCs for the redshift of the background source are plotted in red and yellow, respectively. The green circles mark the constraints, and the magenta circles show the model-predicted image locations. Each image is $1\rlap{.}'0$ (except for the bottom left panel, which is $2\rlap{.}'0$) on a side with a resolution of $0\rlap{.}''09$ pixel^{-1}. Top row: P-SHMs. Each of these models predicts lensed images at their observed locations. Bottom row: F-SHMs. The primary reasons for rejecting these models are as follows. In the bottom left panel, the lensing configuration, arc curvature, and unrealistically high ellipticity of the SHM halo suggest that there is a contribution from a secondary mass halo, which cannot be well represented by an SHM. In the bottom middle panel, the SHM critical curves are extremely large, leading to an unphysical mass distribution for the lensing configuration and producing projections where no arcs are found outside the shown field of view, indicated by the magenta arrow. In the bottom right panel, the SHM predicts lensed images where no arcs are found.

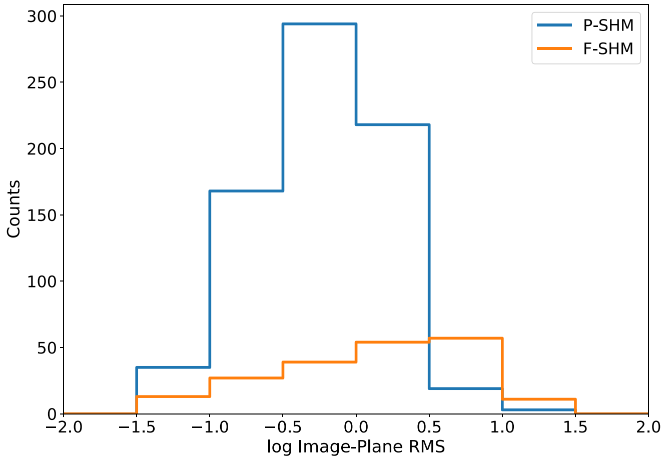

Figure 2. Distribution of the image plane rms of the lens models. The distributions of P-SHMs and F-SHMs in the visual inspection are shown in blue and orange, respectively. The F-SHM distribution is skewed toward higher rms values, but both F-SHMs and P-SHMs can have low rms values, making this an insufficient predictor of model quality.

high-mass bin, the core mass is highly overestimated; we explain this bias below.

In Figure 4, we separate the sample into two bins according to their pass/fail assessment (see Section 4.3). We find that the P-SHMs span a tighter core mass range compared to the F-SHMs; i.e., SHMs in the high- and low-mass bins are more likely to fail. In all mass bins, the core masses computed from the F-SHM models are less accurate; in particular, the large scatter observed in the high-mass bin in Figure 3 is due entirely to F-SHM models. Overall, the mass estimate of the P-SHMs has a scatter of 3.26% with a bias of 0.34% compared to the true mass. This result implies that the larger scatter and bias of the whole sample are driven by the F-SHM lines of sight.

Further investigation of these catastrophic failures highlights the limitation of SHMs in recovering some underconstrained lensing configurations. We find that in most of the high-mass, highly overestimated cases, the SHM converges on a solution where the halo is oriented such that the single giant arc forms on a critical curve in the direction of its semiminor axis, rather than in the direction of its semimajor axis. An example of such

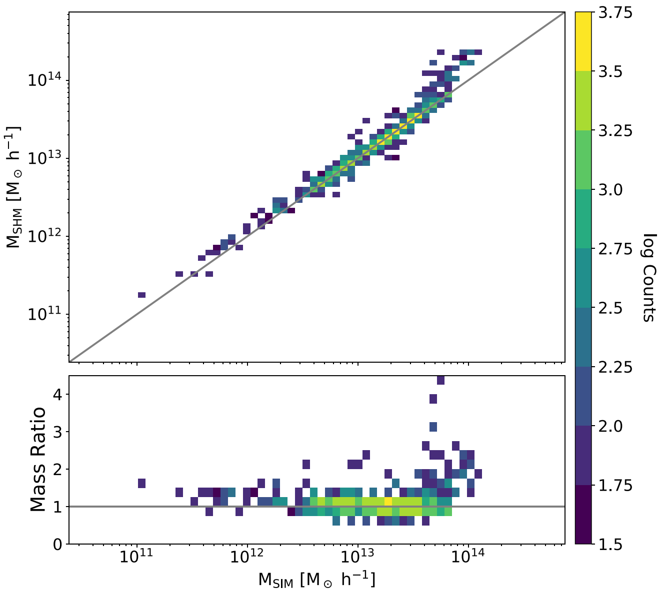

Figure 3. Mass comparison between $M_{\rm SHM}$ and $M_{\rm SIM}$. Top panel: direct comparison between the aperture mass enclosed by $e\theta_{\rm E}$ ($M_{\rm SHM}$) and the "true" aperture mass within the same aperture from the simulation surface density ($M_{\rm SIM}$). The solid gray line is where $M_{\rm SHM} = M_{\rm SIM}$, plotted to guide the eye. Bottom panel: mass ratio, $M_{\rm SHM}/M_{\rm SIM}$. We find that, on average, $M_{\rm SHM}$ overestimates $M_{\rm SIM}$, especially in the high-mass bins (see Section 5).

a failed model is shown in the bottom middle panel of Figure 1. These models populate the highest core mass bin in Figure 3, since they produce a large $e\theta_E$, and they overestimate the mass, since the model converges on a wrong solution, perpendicular to the underlying mass distribution. Fortunately, these cases are easily identified in a visual inspection. In analyses of real data, these cases can be flagged for a more involved analysis beyond the automated SHM. Manually imposing more constrained priors, increasing the complexity of the model, or adding constraints from secondary lensed systems may resolve these cases.

All of these indicate that a quick visual inspection of the model outputs is beneficial when estimating the mass at the cores of galaxy clusters using the SHM method.

5.1. Possible Causes of Scatter and Bias in the M_{SHM} *Mass Estimate*

We explore possible dependencies in the scatter and bias of $M_{\rm SHM}$ with respect to $M_{\rm SIM}$ against the SHM best-fit parameters (velocity dispersion (σ), ellipticity (ϵ), and core radius ($R_{\rm core}$)). The results are shown in Figure 5. When considering the entire sample (including F-SHMs), we find that the scatter is larger at small and large ϵ, $e\theta_{\rm E}$, and large values of $R_{\rm core}$.

For P-SHMs (plotted in orange for comparison), we find no trends in the scatter or bias with any of the model parameters. This plot clearly shows the reduction in the scatter and bias in the P-SHMs when compared to all SHMs.

The large scatter and high occurrence of F-SHMs found in the extreme values of the SHM fit parameters—σ, ϵ, and $R_{\rm core}$—indicate that during the minimization process, the best-fit model was found at the edge of the parameter space. These cases require additional human attention, better parameter exploration, and possibly an increase in the flexibility of the model. These interventions are not allowed in the framework of an automated SHM but are common practice in detailed lensing analyses. The increase in the complexity of the model is usually met with a need for additional constraints. It is expected that the SHM will struggle to reproduce dark matter halos with significantly disturbed morphology or mergers and converge on, e.g., the highest ellipticity allowed, as shown in the bottom left panel of Figure 1.

We also test the results against the rmsi in order to determine whether it could serve as a quantitative indicator of model quality (Figure 6(e)). As expected, we find large scatter and bias in the high-rmsi bin, attributed to F-SHMs. However, we also find that both all SHMs and the P-SHMs have high scatter in the lowest-rmsi bin (rms $\approx 1\farcs0$). This behavior is consistent with previous studies. For example, Johnson & Sharon (2016) showed that a larger number of constraints lead to better accuracy in recovering the underlying mass and magnification, while the rmsi becomes worse. The trend of increased scatter with decreased rmsi and the fact that some F-SHMs have low rmsi both indicate that the rmsi does not provide a good indicator of model quality. However, high rmsi values may be useful as an initial triage to remove some of the catastrophic failures before visual inspection.

For reference, if excluding models with log(rmsi) > 0.5, the scatter and bias reduce to 4.8% and 0.65%, respectively, better than the overall sample (8.52%, 0.90%) but not as good as the P-SHM sample (3.26%, 0.34%).

Next, we explore whether the scatter and bias depend on the properties of the simulated galaxy cluster total mass (M_{200c}), concentration (c_{200c}), cluster redshift ($z_{\rm L}$), and background source redshift ($z_{\rm S}$). The results are shown in Figure 6. We find a flat trend in the scatter and bias with respect to all of the cluster and background source properties for both the SHMs (including F-SHMs) and P-SHMs. This exploration of the scatter and bias is crucial for future studies that may use the $M_{\rm SHM}$ method to measure the core mass and combine it with a large-scale mass proxy to measure, e.g., the concentration of an ensemble of galaxy clusters. Based on this result, we conclude that using $M_{\rm SHM}$ to measure core masses will not bias such future work.

6. The Effect of the Background Source Redshift and the Lensing Configuration of the Arcs

In this section, we investigate the effect on the SHM and the aperture mass enclosed by the effective Einstein radius of the SHM due to the background source redshift, lensing configuration of the arcs, and addition of a second lensed image system. Here we do not exclude the F-SHMs from the analysis.

6.1. Effects of the Background Source Redshift (z_S) on M_{SHM}

When a secure spectroscopic redshift of a lensed galaxy is not available, lens modelers often leave the source redshift as a free parameter, sometimes using its photometric redshift as prior. By leaving the background source redshift as a free parameter in our test models, the number of degrees of freedom increases to seven, requiring seven or more constraints. This is satisfied by 895 ray-traced images in our overall simulated sample. We apply a broad uniform prior on the background source redshift, $1 \leqslant z_{\rm S} \leqslant 5$. From the computed models, we find that the model-predicted redshifts are, on average, 1.9 times higher than the true redshifts. We measure a scatter of 9.85% with a bias of -7.22% on the mass estimate $M_{\rm SHM}$. The $M_{\rm SHM}$,

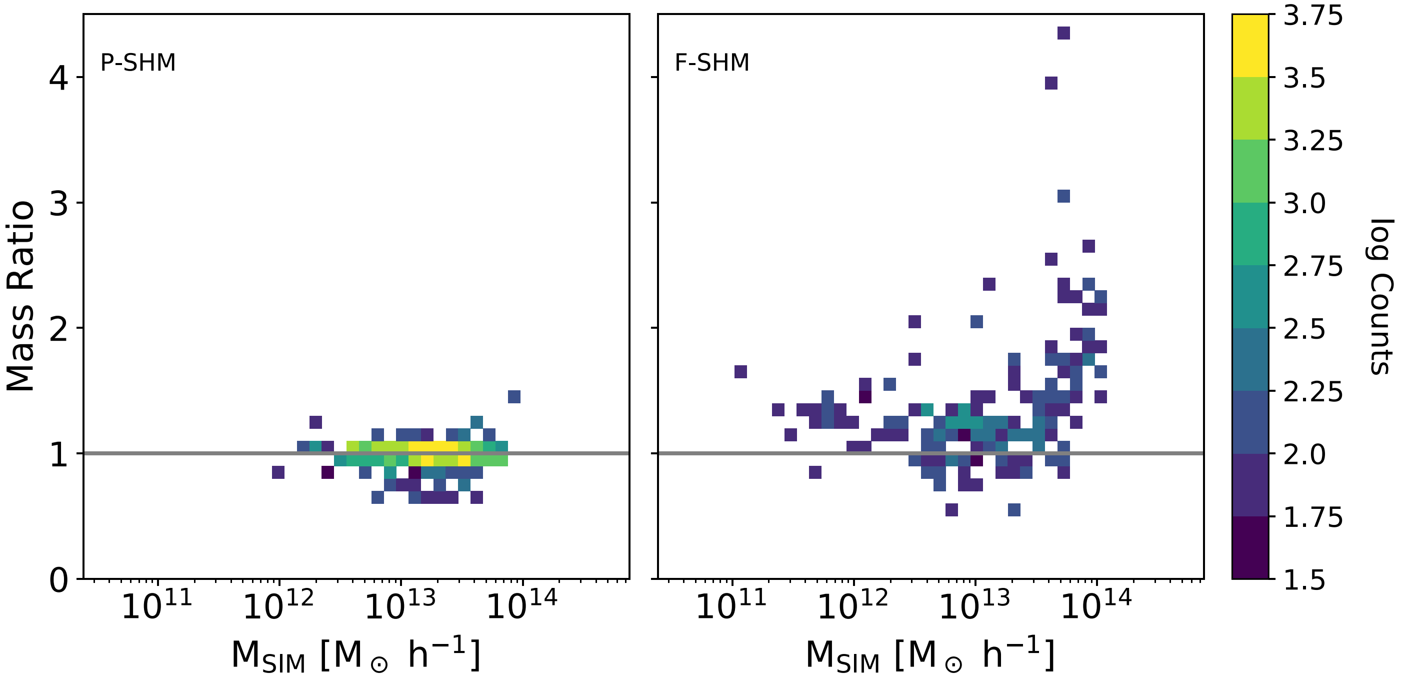

Figure 4. Comparison between the mass estimates of P-SHMs and F-SHMs. The mass ratio ($M_{\rm SHM}/M_{\rm SIM}$) of the P-SHMs is plotted in the left panel, and that of the F-SHMs is plotted in the right panel. The P-SHMs span a somewhat smaller mass range than the F-SHMs. Notably, on average, the F-SHMs are biased high, and their spread about the one-to-one line is higher than that of the P-SHMs, indicating that a quick visual inspection of the SHM outputs can easily weed out most of the outliers.

when no background source redshift is known, underestimates the true aperture mass enclosed by the effective Einstein radius, and the scatter increases. This effect shows the degeneracy between the derived mass and the background source redshift and highlights the importance of securing spectroscopic redshifts of background sources for the accuracy of lens models.

6.2. *Effects of the Lensing Configuration on* M_{SHM}

We explore the effect of the lensing configuration of the simulated images on the accuracy of the SHMs, as different configurations provide different constraining power. We inspect each of the simulated lensed images and sort them into eight groups of similar lensing geometry. A representative example of each of the groups is shown in Figure 7, along with the number of simulated images in each group. Systems in group A typically have five images: a merging pair forming a tangential arc, a counterimage, and a clearly observable pair of radial arcs. Systems in group B show a single merging tangential arc and a clearly observable pair of radial arcs. Systems in group C have a similar configuration to group A, without visible radial arcs. Systems in group D have a single arc similar to group B but without visible radial arcs. Systems in group E have a tangential arc made of a merging pair and a counterimage, but unlike group A, only a single radial arc is identified. Group F includes the Einstein ring configuration. Systems in group G have a set of radial and tangential arcs close to each other and an additional counterimage. Group H systems form a merging pair of radial arcs and a single tangential arc.

The SL configuration group that has the most F-SHMs is group D (a single tangential arc); out of the 161 lensed images with this configuration, 117 (∼73%) are F-SHMs and 44 (∼27%) are P-SHMs. This group accounts for more than half of the 201 total F-SHMs. This lensing configuration, of a single giant arc, provides the least geometrical constraining power, as it leaves regions of the lens plane with no constraints. Since the model is only locally constrained, lensing configurations in which the single halo is oriented approximately perpendicular to the orientation of the underlying mass distribution are allowed; models that have constraints only on one side of the center of mass suffer from high degeneracy between the halo position, its ellipticity, and velocity dispersion. Such low constraining power is also reported in some observed systems with single giant arcs in Sharon et al. (2020). The low constraining power can therefore result in unphysical SHMs and an unreliable measurement of the mass enclosed by the effective Einstein radius. Excluding the 161 single-arc images from the full sample, the scatter and bias reduce to 3.88% and 0.84%, respectively, significantly improving upon the scatter of the full sample (scatter: 8.52%; bias: 0.90%) and close to the precision of the P-SHM-only sample (scatter: 3.26%; bias: 0.34%).

Some of the challenges inherent to using a single giant arc as the only constraint can be mitigated by obtaining more lensing constraints (see Section 6.3), which often requires higher resolution or deeper imaging. Some of these failed cases can be recovered with a more involved analysis, manual inspection of the parameter space, or inclusion of physically motivated priors (such as an upper limit on the velocity dispersion–based cluster richness). As noted in Section 5.1, these interventions are beyond the framework of the quasi-automated SHM.

6.3. *Constraining Power of Secondary Lensed Image Systems*

Last, we investigate the constraining power of a secondary lensed source system. The SHM benefits from the addition of a

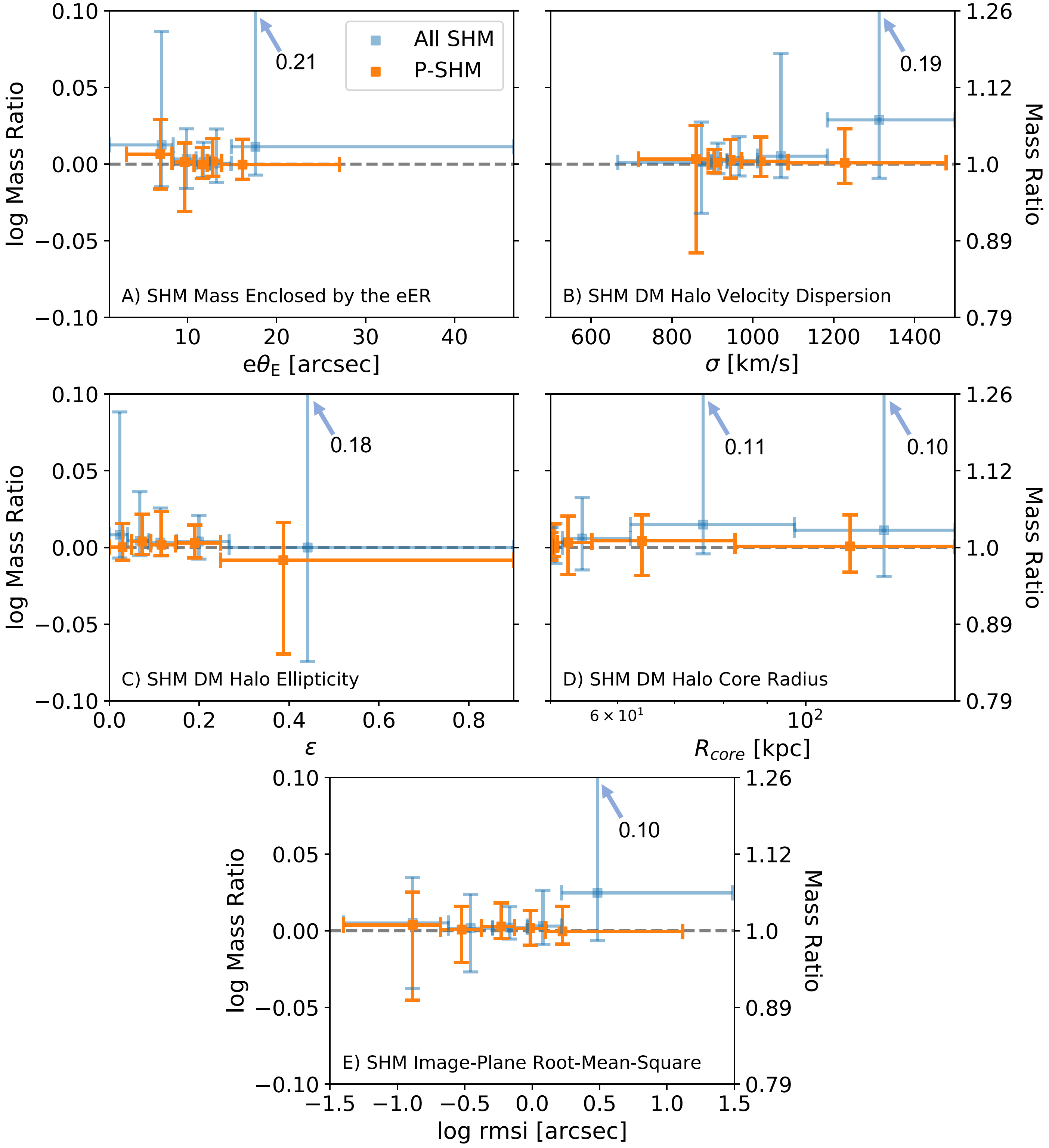

Figure 5. Mass ratio ($M_{\rm SHM}/M_{\rm SIM}$) binned by the SHM best-fit parameters. Shown are the mass ratio binned by the effective Einstein radius ($e\theta_{\rm E}$; panel (a)), dark matter halo model velocity dispersion (σ; panel (b)), dark matter halo model ellipticity (ϵ; panel (c)), dark matter halo model core radius ($R_{\rm core}$; panel (d)), and image plane rms (panel (e)). The square symbol marks the median of the distribution of the mass ratio, the horizontal error bars indicate the bin size (selected such that there is an equal number of SHMs per bin), and the vertical error bars represent the 16th and 84th percentiles. We plot the results for all SHMs (blue) and only P-SHMs (orange) for comparison. We find that the P-SHMs have no bias and a smaller scatter than the uninspected sample (all SHMs). Without eliminating the failed models, the scatter is higher overall; it increases with the extreme (low and high) values of the model parameters. See Section 5.1 for discussion.

lensed system when these new constraints complement the geometrical constraints of the primary image system and the mass distribution. The increase in constraining power at the core of the galaxy cluster benefits lensed systems with a single giant arc (group D) where the arc coverage is limited to one side of the cluster.

For example, when adding a secondary lensed system (of any non-D group) to failed lens models of group D, 53% of

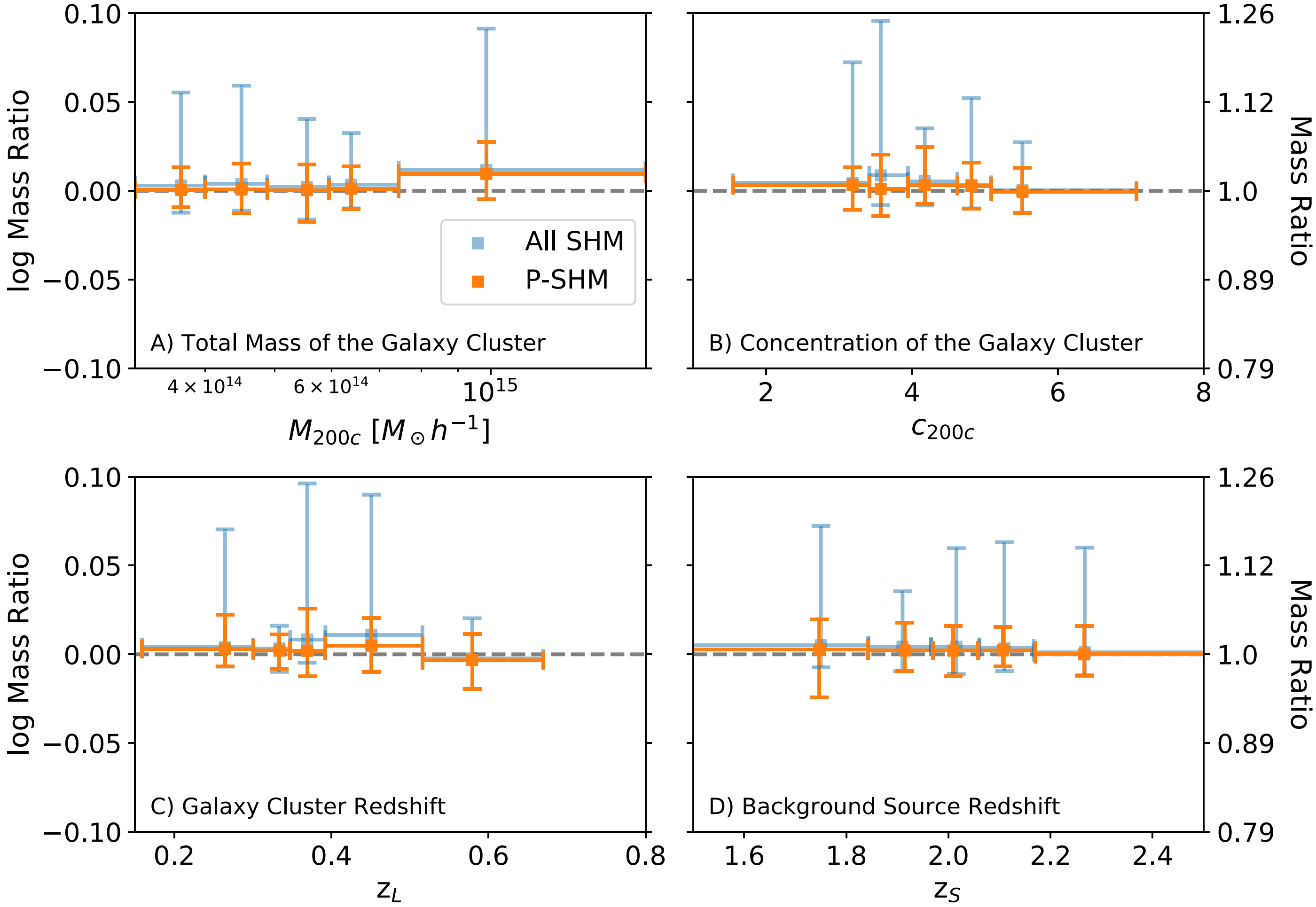

Figure 6. Mass ratio ($M_{\mathrm{SHM}}/M_{\mathrm{SIM}}$) binned by the lens background source system properties. The mass ratio binned by the total mass (M_{200c}; panel (a)), concentration (c_{200c}; panel (b)), galaxy cluster redshift (z_{L}; panel (c)), and background source redshift (z_{S}; panel (d)) are plotted for all SHMs (blue) and the P-SHMs (orange). The square symbol marks the median of the distribution of the mass ratio, the horizontal error bars indicate the bin size (equal number of SHMs per bin), and the vertical error bars represent the 16th and 84th percentile. We find no trend in the scatter and bias with respect to any of the simulated cluster and background source properties for neither all SHMs nor P-SHMs.

these formerly F-SHMs pass the visual inspection and become P-SHMs. This behavior illustrates the importance of identifying additional lensed images to help constrain the lens models. On the other hand, about a third of the failed D models did not benefit from adding a secondary system, even though the SHM produced a passing model when using only that second system as constraints. A further inspection of these failed models indicates that in these particular cases, the lensing geometry of the D arc was so hard for an SHM to reproduce that it forced the model to converge on a failed solution. Such configurations will likely require more involved lensing analysis, possibly with higher flexibility in the lens model or imposing user-identified priors beyond the automated SHM process.

7. Conclusions

We explore the use of SHMs as an automated tool to efficiently estimate the mass at the core of SL galaxy clusters. The SHM can be automatically computed once the arcs have been identified and background source redshift measured. This method uses the parametric lensing algorithm `Lenstool` with a single dark matter halo, represented by a dPIE. The constraints used are the lens redshift, the positions of the lensed images, and their source redshift. An initial halo center position (e.g., the BCG) is also needed as input. To characterize the scatter and bias in the estimator, we use ray-traced simulated images from the state-of-the-art Outer Rim simulation. We compute the SHM, measure the aperture mass enclosed by the effective Einstein radius (M_{SHM}), and compare the mass estimate to the mass from the simulation, measured within the same aperture (M_{SIM}). We conclude the following.

1. Considering the entire sample, the scatter of M_{SHM} is 8.52% with a bias of 0.90% compared to the true mass, M_{SIM}.
2. A quick visual inspection of the SHMs reveals that some fail to reproduce the lensing configuration or lead to unphysical lens models. Excluding the F-SHMs reduces the scatter and bias to 3.26% and 0.34%, respectively.
3. We find that the scatter is larger at small and large values of the ellipticity (ϵ) and effective Einstein radius ($e\theta_{\mathrm{E}}$) and large values of the core radius (R_{core}). Excluding the F-SHMs eliminates this trend.
4. We find a weak increasing trend in the bias with the SHM velocity dispersion (σ) and a larger scatter at larger σ. Excluding the F-SHMs eliminates this trend.
5. We find no significant dependence on the bias and scatter of M_{SHM} with respect to the properties of the lens-source

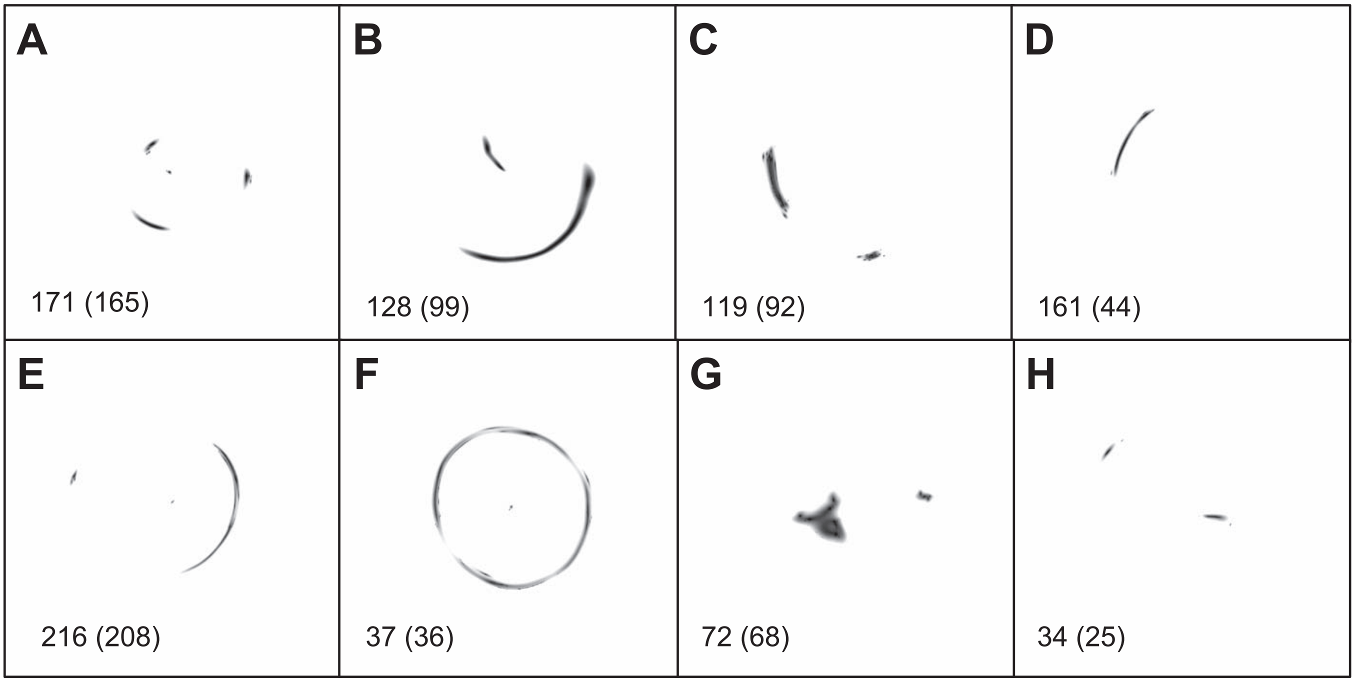

Figure 7. The SL geometric configurations of arcs. Shown are examples of the groups of the simulated SL geometric configurations of the arcs. Each image is 1′.0 on a side. In the bottom left corner of every panel, we indicate the total number of simulated images in that group and, in parentheses, the number of SHMs that pass visual inspection. See Section 6.2 for a description of the different groups.

system: total mass, concentration, lens redshift, and source redshift. This exploration is crucial for future studies that may use the $M_{\rm SHM}$ method to measure the core mass and combine it with a large-scale mass proxy to measure, e.g., the concentration of an ensemble of galaxy clusters. Based on this result, we conclude that using $M_{\rm SHM}$ to measure core masses will not bias such future work.

6. A high rms can be used to identify and eliminate some of the worst cases of F-SHM before the visual inspection; but on its own, it is an insufficient predictor of the SHM model quality.
7. When the background source redshift is unknown, lens modelers frequently use priors on the source redshift and set the redshift as a free parameter in the lens model. We use a broad uniform prior on the source redshift and find that the model-predicted redshifts are overestimated, leading to an underestimate of the mass. When the source redshift is unknown, the scatter and bias $M_{\rm SHM}$ are 9.85% and −7.22% compared to $M_{\rm SIM}$, respectively. Our analysis affirms the importance of securing spectroscopic redshifts or high-quality photometric redshifts for the lensing constraints in order to obtain a precise and accurate mass measurement. This is consistent with findings by, e.g., Caminha et al. (2016) and Johnson & Sharon (2016).
8. The lensing configuration affects the efficacy of the SHM. We find that a single-arc configuration (group D) provides the least constraining power and accounts for most of the extreme outliers. Excluding these systems, we compute a scatter and bias on $M_{\rm SHM}$ of 3.88% and 0.84% against $M_{\rm SIM}$, respectively.
9. The addition of a second lensed source helps constrain the lens model and particularly benefits lens models where the geometrical configuration of the arcs has limited constraining power at the core of the SL galaxy clusters (group D). It is therefore most cost-effective to follow up systems with a single arc with deeper or high-resolution imaging in order to secure additional lensing constraints. However, some lensing configurations may require a more complex lens modeling process than the SHM.

In the future, new tools will expedite the current manual process of SL analysis. Examples include the introduction of convolutional neural networks for identification of SL features (e.g., Petrillo et al. 2017; Jacobs et al. 2019; Cañameras et al. 2020; Huang et al. 2021) and machine-learning algorithms to model the mass distribution of strong lenses (e.g., Bom et al. 2019; Pearson et al. 2019). We look forward to the continuous development of these tools, as the SHMs introduced in this work will greatly benefit from them.

The evaluation of $M_{\rm SHM}$ presented in this work facilitates the use of this efficient mass estimate at the core of SL galaxy clusters and enables an automated measurement of the core mass in the large samples of SL clusters from current and future surveys.

The authors would like to thank the anonymous referee for insightful suggestions that improved this manuscript. This material is based upon work supported by the National Science Foundation Graduate Research Fellowship Program under grant No. DGE 1256260. Work at Argonne National Lab is supported by UChicago Argonne LLC, Operator of Argonne National Laboratory. Argonne National Lab, a U.S. Department of Energy Office of Science Laboratory, is operated by UChicago Argonne LLC under contract No. DE-AC02-06CH11357. This research used resources of the Argonne Leadership Computing Facility, which is a DOE Office of Science User Facility supported under contract DE-AC02-

06CH11357. G.M. received funding from the European Union's Horizon 2020 research and innovation programme under the Marie Sklodowska-Curie grant agreement No. 896778.

ORCID iDs

J. D. Remolina González https://orcid.org/0000-0002-7868-9827
K. Sharon https://orcid.org/0000-0002-7559-0864
N. Li https://orcid.org/0000-0001-6800-7389
G. Mahler https://orcid.org/0000-0003-3266-2001
L. E. Bleem https://orcid.org/0000-0001-7665-5079
M. Gladders https://orcid.org/0000-0003-1370-5010
A. Niemiec https://orcid.org/0000-0003-3791-2647

References

Acebron, A., Jullo, E., Limousin, M., et al. 2017, MNRAS, 470, 1809
Allen, S. W., Evrard, A. E., & Mantz, A. B. 2011, ARA&A, 49, 409
Amendola, L., Appleby, S., Avgoustidis, A., et al. 2018, LRR, 21, 2
Bayliss, M. B., Gladders, M. D., Oguri, M., et al. 2011, ApJL, 727, L26
Bayliss, M. B., Johnson, T., Gladders, M. D., Sharon, K., & Oguri, M. 2014, ApJ, 783, 41
Benson, B. A., Ade, P. A. R., Ahmed, Z., et al. 2014, Proc. SPIE, 9153, 91531P
Bleem, L. E., Bocquet, S., Stalder, B., et al. 2020, ApJS, 247, 25
Bleem, L. E., Stalder, B., de Haan, T., et al. 2015, ApJS, 216, 27
Bocquet, S., Dietrich, J. P., Schrabback, T., et al. 2019, ApJ, 878, 55
Bocquet, S., Heitmann, K., Habib, S., et al. 2020, ApJ, 901, 5
Bom, C., Poh, J., Nord, B., Blanco-Valentin, M., & Dias, L. 2019, arXiv:1911.06341
Broadhurst, T. J., & Barkana, R. 2008, MNRAS, 390, 1647
Caminha, G. B., Grillo, C., Rosati, P., et al. 2016, A&A, 587, A80
Cañameras, R., Schuldt, S., Suyu, S. H., et al. 2020, A&A, 644, A163
Cerny, C., Sharon, K., Andrade-Santos, F., et al. 2018, ApJ, 859, 159
Child, H. L., Habib, S., Heitmann, K., et al. 2018, ApJ, 859, 55
Chirivì, G., Suyu, S. H., Grillo, C., et al. 2018, A&A, 614, A8
Corless, V. L., & King, L. J. 2009, MNRAS, 396, 315
D'Aloisio, A., Natarajan, P., & Shapiro, P. R. 2014, MNRAS, 445, 3581
Diego, J. M., Broadhurst, T., Wong, J., et al. 2016, MNRAS, 459, 3447
Duffy, A. R., Schaye, J., Kay, S. T., & Dalla Vecchia, C. 2008, MNRAS, 390, L64
Elíasdóttir, Á., Limousin, M., Richard, J., et al. 2007, arXiv:0710.5636
Evrard, A. E., MacFarland, T. J., Couchman, H. M. P., et al. 2002, ApJ, 573, 7
Gonzalez, A. H., Stanford, S. A., Brodwin, M., et al. 2012, ApJ, 753, 163
Gonzalez, E. J., Chalela, M., Jauzac, M., et al. 2020, MNRAS, 494, 349
Gralla, M. B., Sharon, K., Gladders, M. D., et al. 2011, ApJ, 737, 74
Habib, S., Pope, A., Finkel, H., et al. 2016, NewA, 42, 49
Heitmann, K., Finkel, H., Pope, A., et al. 2019, ApJS, 245, 16
Hilbert, S., White, S. D. M., Hartlap, J., & Schneider, P. 2007, MNRAS, 382, 121
Hilbert, S., White, S. D. M., Hartlap, J., & Schneider, P. 2008, MNRAS, 386, 1845
Hilton, M., Hasselfield, M., Sifón, C., et al. 2018, ApJS, 235, 20
Hu, W. 2003, PhRvD, 67, 081304
Huang, N., Bleem, L. E., Stalder, B., et al. 2020, AJ, 159, 110
Huang, X., Storfer, C., Gu, A., et al. 2021, ApJ, 909, 27
Huterer, D., & Shafer, D. L. 2018, RPPh, 81, 016901
Jacobs, C., Collett, T., Glazebrook, K., et al. 2019, ApJS, 243, 17
Jauzac, M., Klein, B., Kneib, J.-P., et al. 2020, arXiv:2006.10700
Jenkins, A., Frenk, C. S., White, S. D. M., et al. 2001, MNRAS, 321, 372
Johnson, T. L., Rigby, J. R., Sharon, K., et al. 2017a, ApJL, 843, L21
Johnson, T. L., & Sharon, K. 2016, ApJ, 832, 82
Johnson, T. L., Sharon, K., Bayliss, M. B., et al. 2014, ApJ, 797, 48
Johnson, T. L., Sharon, K., Gladders, M. D., et al. 2017b, ApJ, 843, 78
Jullo, E., Kneib, J. P., Limousin, M., et al. 2007, NJPh, 9, 447
Kawamata, R., Oguri, M., Ishigaki, M., Shimasaku, K., & Ouchi, M. 2016, ApJ, 819, 114
Khedekar, S., & Majumdar, S. 2013, JCAP, 2013, 030
Khullar, G., Gozman, K., Lin, J. J., et al. 2020, ApJ, 906, 107
Komatsu, E., Smith, K. M., Dunkley, J., et al. 2011, ApJS, 192, 18
Lagattuta, D. J., Richard, J., Bauer, F. E., et al. 2019, MNRAS, 485, 3738
Laureijs, R., Amiaux, J., Arduini, S., et al. 2011, arXiv:1110.3193
Li, N., Gladders, M. D., Heitmann, K., et al. 2019, ApJ, 878, 122
Li, N., Gladders, M. D., Rangel, E. M., et al. 2016, ApJ, 828, 54
LSST Science Collaboration, Abell, P. A., Allison, J., et al. 2009, arXiv:0912.0201
LSST Science Collaboration, Marshall, P., Anguita, T., et al. 2017, arXiv:1708.04058
Lotz, J. M., Koekemoer, A., Coe, D., et al. 2017, ApJ, 837, 97
Mahler, G., Richard, J., Clément, B., et al. 2018, MNRAS, 473, 663
Mahler, G., Sharon, K., Gladders, M. D., et al. 2020, ApJ, 894, 150
Mantz, A. B., Allen, S. W., Morris, R. G., et al. 2014, MNRAS, 440, 2077
Marriage, T. A., Acquaviva, V., Ade, P. A. R., et al. 2011, ApJ, 737, 61
Meneghetti, M., Bartelmann, M., Dahle, H., & Limousin, M. 2013, SSRv, 177, 31
Meneghetti, M., Bartelmann, M., & Moscardini, L. 2003, MNRAS, 346, 67
Meneghetti, M., Natarajan, P., Coe, D., et al. 2017, MNRAS, 472, 3177
Meneghetti, M., Rasia, E., Vega, J., et al. 2014, ApJ, 797, 34
Merten, J., Meneghetti, M., Postman, M., et al. 2015, ApJ, 806, 4
Mittal, A., de Bernardis, F., & Niemack, M. D. 2018, JCAP, 2018, 032
Nord, B., Buckley-Geer, E., Lin, H., et al. 2016, ApJ, 827, 51
Nord, B., Buckley-Geer, E., Lin, H., et al. 2020, MNRAS, 494, 1308
Oguri, M. 2006, MNRAS, 367, 1241
Oguri, M., Bayliss, M. B., Dahle, H., et al. 2012, MNRAS, 420, 3213
Oguri, M., & Blandford, R. D. 2009, MNRAS, 392, 930
Paterno-Mahler, R., Sharon, K., Coe, D., et al. 2018, ApJ, 863, 154
Pearson, J., Li, N., & Dye, S. 2019, MNRAS, 488, 991
Petrillo, C. E., Tortora, C., Chatterjee, S., et al. 2017, MNRAS, 472, 1129
Pillepich, A., Reiprich, T. H., Porciani, C., Borm, K., & Merloni, A. 2018, MNRAS, 481, 613
Pratt, G. W., Arnaud, M., Biviano, A., et al. 2019, SSRv, 215, 25
Priewe, J., Williams, L. L. R., Liesenborgs, J., Coe, D., & Rodney, S. A. 2017, MNRAS, 465, 1030
Raney, C. A., Keeton, C. R., & Brennan, S. 2020a, MNRAS, 492, 503
Raney, C. A., Keeton, C. R., Brennan, S., & Fan, H. 2020b, MNRAS, 494, 4771
Rangel, E., Li, N., Habib, S., et al. 2016, in 2016 IEEE Int. Conf. on Cluster Computing (CLUSTER) (Piscataway, NJ: IEEE), 30
Remolina González, J. D., Sharon, K., & Mahler, G. 2018, ApJ, 863, 60
Remolina González, J. D., Sharon, K., Reed, B., et al. 2020, ApJ, 902, 44
Richard, J., Kneib, J.-P., Ebeling, H., et al. 2011, MNRAS, 414, L31
Rigby, J. R., Bayliss, M. B., Sharon, K., et al. 2018, AJ, 155, 104
Sebesta, K., Williams, L. L. R., Liesenborgs, J., Medezinski, E., & Okabe, N. 2019, MNRAS, 488, 3251
Sharon, K., Bayliss, M. B., Dahle, H., et al. 2020, ApJS, 247, 12
Shin, T., Adhikari, S., Baxter, E. J., et al. 2019, MNRAS, 487, 2900
Strait, V., Bradač, M., Hoag, A., et al. 2018, ApJ, 868, 129
Umetsu, K., & Diemer, B. 2017, ApJ, 836, 231
Verdugo, T., Motta, V., Muñoz, R. P., et al. 2011, A&A, 527, A124
Wambsganss, J., Bode, P., & Ostriker, J. P. 2004, ApJL, 606, L93
Wambsganss, J., Ostriker, J. P., & Bode, P. 2008, ApJ, 676, 753
Zitrin, A., Zheng, W., Broadhurst, T., et al. 2014, ApJL, 793, L12